Order by Inertia in Spinning Active Matter: Holey Fluids and Spin-Textured Crystals

Camille Jorge[1,2] and Denis Bartolo[1,*]

[1]*CNRS, ENS de Lyon, LPENSL, UMR5672, 69342, Lyon cedex 07, France*
[2]*Institute of Physics, University of Amsterdam, Science Park 904, 1098 XH, Amsterdam, The Netherlands*

(Received 18 May 2026; accepted 22 September 2026; published 6 November 2026)

Active matter sustains emergent flows at the expense of preserving structural order. The feedback between structure and viscous flows typically disrupts crystalline and liquid-crystalline organization by amplifying the very deformations they generate. Yet this destabilizing paradigm has recently been challenged by experiments showing that inertial fluid flows can stabilize few-body bound states of active spinners. Whether inertial active matter can sustain genuine cohesion and order at the many-body level, however, remains elusive. Here we investigate two-dimensional assemblies of macroscopic spinners operating at high Reynolds number and uncover two phase transitions leading to the emergence of a dilute percolating fluid and a dense spin-textured crystal. At low density, inertial flows generate two competing interactions: anisotropic attractions and transverse Magnus forces that continuously break and reconfigure bonds. Together they drive a percolation transition toward a dynamically rearranging holey liquid reminiscent of the empty-liquid states observed in equilibrium patchy colloids. At high density, the feedback between spin alignment and particle positions suppresses transverse rearrangements and yields a first-order transition toward a spin-ordered crystal. Our results demonstrate that, beyond the overdamped limit, hydrodynamic feedback can promote rather than destroy collective order, revealing a distinct regime of many-body active matter governed by inertial flows.

DOI: 10.1103/xyym-pjh7

Subject Areas: Soft Matter, Statistical Physics

At equilibrium, the spatial organization of matter is immune to the details of its dynamics. Whether microscopic motion is inertial or viscous, thermal statistics governs structure, and phase behavior does not depend on how fast fluctuations propagate and relax. This protection is lost once matter is driven out of equilibrium, where structure and flow become intertwined. In homogeneously driven soft matter, deformations generate flows that can either amplify or suppress them, leading to dynamically organized or disordered steady states in systems ranging from sedimenting suspensions to synthetic and living spinner crystals [1–12]. Yet the forcing itself remains fixed: structural rearrangements and flows do not reorient gravity, the chirality of living cells or the magnetic field that drives the system.

Soft active matter features a more intimate form of nonequilibrium, where actuation, flow, and structure are two-way coupled: the forces and stresses that drive the system from within are themselves shaped by the deformations they induce. In the viscous regime, this interplay is most often destabilizing: distortions of ordered active phases generate flows that amplify them, as strikingly illustrated by the spatiotemporal chaos of active nematics, gels, and swimmer suspensions [13–17]. Hydrodynamic interactions tend to suppress long-range order in soft active matter. Recent observations of active spinners operating at finite Reynolds number contrast with this seemingly general destabilization by revealing stable bound states sustained by inertial vortices [18–20]. Whether such inertia-mediated interactions can stabilize cohesive and ordered phases of spinning active matter remains unknown.

To determine whether inertial feedback can stabilize cohesive many-body organization, we investigate an assembly of hydrodynamically interacting spinners operating at finite Reynolds number. Through quantitative measurements of positional and active-spin correlations, we show that inertial forces and viscous torques produce a two-way coupling between positional and spin degrees of freedom that shapes the phase behavior. By systematically varying the packing fraction, we demonstrate that the system evolves through three distinct steady states separated by two phase transitions: a liquid of fractal clusters, a dynamically rearranging holey fluid, and a

*Contact author: denis.bartolo@ens-lyon.fr

Published by the American Physical Society under the terms of the Creative Commons Attribution 4.0 International license. Further distribution of this work must maintain attribution to the author(s) and the published article's title, journal citation, and DOI.

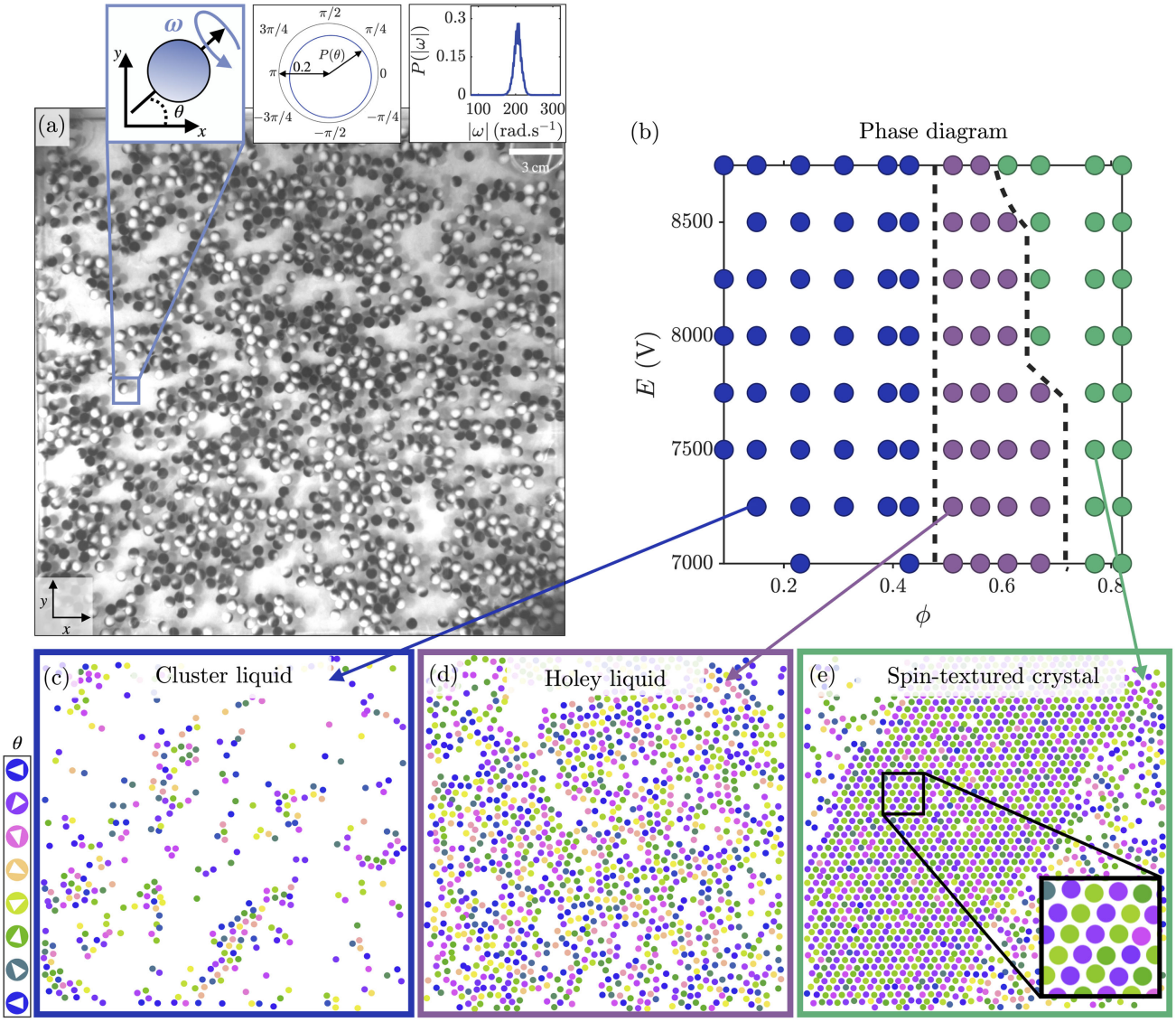


FIG. 1. Active spinners, cluster liquid, percolating fluid, and spin-textured crystal. (a) Experimental picture illustrating the spinning motion of a system of spherical plastic beads motorized using Quincke electrorotation ($\phi = 0.51$). Painting the beads surfaces allows us to monitor their instantaneous spinning rate ω. See also Supplemental video 1 [21]. Left inset: scheme of a bead of spin $\boldsymbol{\omega}$ forming an angle θ with the horizontal. Middle inset: probability density of θ. At low packing fraction, all particles spin along random directions. ($E = 8750$ V). Right inset: probability density of $|\omega|$. The rotation speed is constant ($E = 8750$ V and $\phi = 0.39$). (b) Phase diagram constructed from 97 different experiments. The three phases are mostly determined by the spinners packing fraction. The phase boundaries hardly depend on the magnitude of the voltage E. (c),(d), and (e) Snapshots of three instantaneous spinner configurations recorded at three different packing fractions. The particles are colored according to their instantaneous orientation. See also Supplemental videos 2, 3, and 4 [21]. (c) $\phi = 0.15$: The spinners form an isotropic liquid of clusters. (d) $\phi = 0.51$: The spinners form an isotropic percolating fluid. Unlike in colloidal gels [31,32], their structure is highly dynamical. (e) $\phi = 0.67$: The active particles phase separate into a spin-textured crystals where spins form ferromagnetic lines along a principal axis of the crystal and alternate orientation from one line to the next. The crystal coexists with a dilute cluster liquid.

dense spin-textured crystal. Remarkably, as we show below, inertial pumping and Magnus forces generate directed interactions between spinners, providing a hydrodynamic analog of the directional interactions that govern the phase behavior of equilibrium patchy colloids. At high density, however, the feedback between positional and orientational degrees of freedom collapses the holey fluid into a spinner crystal, where particle positions and spinning directions self-organize in unison. Beyond the specifics of our system, our results reveal how inertial hydrodynamic flows transform the destabilizing feedback typical of overdamped active matter into a mechanism of phase ordering at the many-body level.

I. ACTIVE SPINNER EXPERIMENTS

We detail the experimental setup shown in Fig. 1(a) in Supplemental Material [21]. In brief, we confine plastic beads of radius $a = 3$ mm immersed in a hexadecane solution between two transparent electrodes separated by 8.5 mm and apply a dc electric field along $\hat{\mathbf{z}}$ to activate Quincke electrorotation [27] [Fig. 1(a)]. As in colloidal-roller experiments [28], once the voltage exceeds the Quincke threshold $E_Q = 6000$ V the beads roll along the electrodes (see Supplemental Material [21]). However, increasing the voltage further ($E \geq 7000$ V) lifts the particles off the surface [29], suppresses their translational motion, and produces a hovering monolayer of active spinners (Fig. 1, Supplemental videos 1–4, and Supplemental Material [21]). In the following, we focus on this spinning regime and track the active particle positions $\mathbf{r}_i(t)$, and rotation vectors $\boldsymbol{\omega}_i(t)$, which we refer to as the particle spin [Fig. 1(a)]. Unlike in most active spinner experiments and simulations, the spins are not imposed, but instead evolve dynamically through particle interactions [28,30]. Moreover, the $\boldsymbol{\omega}_i$ are not Ising-like variables restricted to a fixed z axis. In our 97 experiments, illustrated in Fig. 1, each particle can rotate about an arbitrary axis in the xy plane at an approximately constant rate. Their magnitude ω_i is narrowly distributed [Fig. 1(a)] and varies between 24 and 34 Hz as we increases E. As a result, the induced flows are associated to Reynolds number $\mathrm{Re} = a^2\omega/\nu$ ranging from 300 to 400, revealing that the spinners operate in an inertia-dominated regime ($\nu = 4.5$ cSt is the kinematic viscosity of the fluid).

A. From cluster liquids to spin-textured crystals

Figure 1(c) and Supplemental video 2 [21] show that dilute ensembles of interacting spinners form an isotropic liquid phase. Even at low packing fraction ($\phi < \phi_p = 0.43$), small clusters continuously assemble and disassemble, indicating effective attractive interactions that cannot classically originate from motility [33–35], as the spinners exhibit nearly no self-propulsion. At intermediate packing fractions ($\phi_p < \phi < \phi_x = 0.67 \pm 0.07$), the fractal clusters undergo a sharp geometrical transition and self-organize into a holey fluid in which most particles belong to a single percolating cluster [Fig. 1(d)]. Unlike colloidal gels [31,36], this holey fluid is not arrested, but continuously rearranges its geometry, as seen in Supplemental video 3 and quantified in Supplemental Material [21]. It is also worth noting that, unlike Quincke rollers, the spinners have a nearly vanishing translational speed. The holey fluid we observe is therefore qualitatively different from the bubbly phases seen in dense phases past motility-induced phase separation (see Supplemental Material [21] for a more quantitative discussion) [37–40].

At $\phi = \phi_x$, the translational and spin-rotational symmetries of the holey fluid are both spontaneously broken. The holey structure collapses into a dense hexagonal crystal that coexists with a dilute cluster liquid [Fig. 1(e) and Supplemental video 4 [21]). Simultaneously, the spins organize into system-spanning ferromagnetic lines whose orientation alternates from one line to the next. We now demonstrate that these three nonequilibrium steady states define a phase diagram where two phase transitions are chiefly controlled by the spinner packing fraction ϕ [Fig. 1(b)].

II. PERCOLATION, PHASE SEPARATION, AND SPIN ORDERING

We begin by showing that the cluster liquid undergoes a percolation transition, leading to a dynamically rearranging state reminiscent of the empty liquids observed in equilibrium patchy colloids [41]. Figures 2(a) and 2(b) show that the mean cluster size increases with the packing fraction ϕ. However, these clusters are not compact droplets of well-defined size. Instead, they form fractal objects characterized by a power-law size distribution [Figs. 2(a) and 2(b)]. We find that the probability P of observing a system-spanning cluster jumps from zero to one at $\phi_p = 0.43$ in Fig. 2(c). Moreover, Fig. 2(a) shows that at ϕ_p the gyration-radius and cluster-size exponents match those expected at the percolation threshold ($\nu = 91/48$ and $\tau = 187/91$) [42–44]. Together, these results establish that the cluster liquid and the holey fluid are two distinct nonequilibrium phases. Despite this geometrical transition, both phases remain isotropic and lack any form of spin order. In each case, the rotation vectors $\boldsymbol{\omega}_i$ display neither macroscopic alignments nor long-range correlations [Fig. 2(d)].

The collapse of the percolating network into a spin-textured crystal belongs to a fundamentally different class of transition. Supplemental Material video 7 [21], shows that this collapse does not happen homogeneously. Instead, a finite-size crystal forms locally from fluctuations before growing over system spanning scales. This dynamics is very similar to the nucleation and growth typically seen when fluids phase separate in and out of equilibrium [34,46]. Furthermore, Fig. 2(e) shows that a crystalline phase coexists with a dilute liquid in which the bond-orientational order parameter ψ_6 remains vanishingly small. Lastly, Figs. 2(f) and 2(g) show that the crystalline area fraction, the correlation length ξ_6 of the ψ_6 field, and the correlation length of the spin orientation ξ_ω all undergo discontinuous variations at $\phi_x = 0.67$. Together, all our observations indicate that the spinner crystallization is consistent with a first-order transition process. Crucially, crystallization coincides with the emergence of long-range spin order throughout the crystal [Fig. 2(h) and Supplemental Material [21]]. This simultaneous breaking

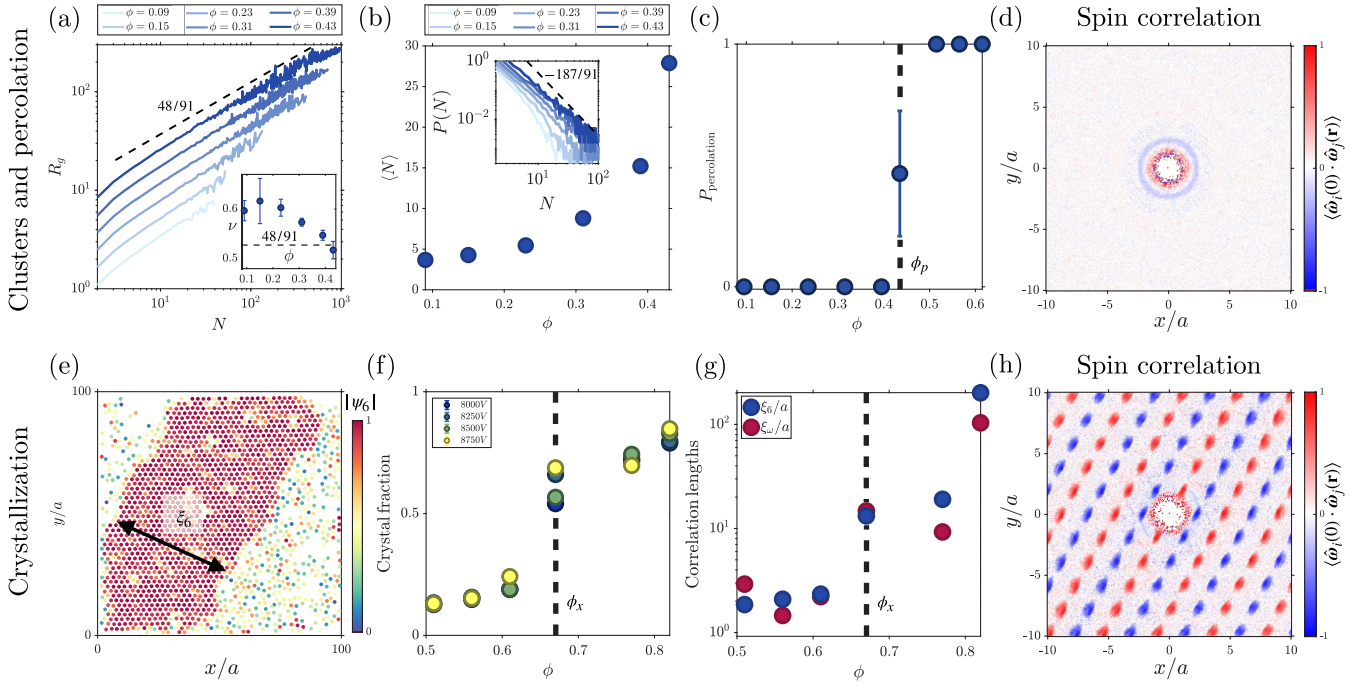


FIG. 2. Percolation transition, phase separation, and spin ordering. (a) The gyration radius of the cluster grows as a power law $R_g \sim N^\nu$ at all packing fractions (all E averaged). Inset: Exponent ν plotted versus ϕ. The dotted line corresponds to the exponent $\nu = 48/91$ computed at the classical percolation transition, see, e.g., [42,45]. (b) The average number of spinners in a cluster $\langle N \rangle$ grows with ϕ (average over all E values). The variations blow up as ϕ approaches $\phi_p = 0.43$. Inset: the sizes of the clusters are power-law distributed. The dashed line corresponds to the power law expected at the percolation transition $\tau = 187/91$ [42,45] (average over all E values). (c) The probability to observe a percolating cluster in an experiment jumps from 0 to 1 at $\phi = \phi_p = 0.43$ ($E = 8250$ V). (d) Typical spin-spin correlations in the holey liquid phase ($E = 7750$ V, $\phi = 0.56$). The spinners only feature very short range isotropic correlations. No long-range spin order builds up. (e) Snapshot of an experiments showing the coexistence between a crystal and a liquid phase. The particles are colored according to the value of their bond orientational order (see Supplemental Material [21]). (f) The area fraction spanned by the crystal phase increases with ϕ and discontinuously jumps at $\phi = \phi_x = 0.67$. (g) The correlation length ξ_6 of the bond-order parameter ϕ_6 measures the extent of the crystals. ξ_ω measures the size of the domain where the spins are collinear. Both ξ_6 and ξ_ω increases sharply at ϕ_x. (h) Spin-spin correlations in the crystal phase. Spins are aligned in the axial direction and anti-aligned from one line to the next. This alternate order persists over system spanning scales ($E = 8750$ V, $\phi = 0.67$).

of translational and spin-rotational symmetries suggests a mutual dependence between positional interactions and spin torques, which we now quantify experimentally.

III. SYMMETRIES OF THE TWO-SPINNER INTERACTIONS

A. Pair correlations

To characterize the symmetries of the pair interactions governing the spinner dynamics, we analyze our experiments in the dilute regime ($\phi < 0.43$), and focus on two central observables. First, we generalize the standard pair-correlation function by conditioning it on the spin orientations of the interacting particles. Specifically, we introduce the spin-resolved two-point distribution $g_{\mathbf{r}}(\mathbf{r}|\theta_1, \theta_2) = P(\mathbf{r}_2 = \mathbf{r}|\mathbf{r}_1 = 0, \theta_1, \theta_2)$, where θ_i denotes the in-plane orientation of the spin vector $\boldsymbol{\omega}_i$ [see Fig. 1(a)]. Measurements are performed in the reference frame where $\mathbf{r}_1 = 0$ and $\boldsymbol{\omega}_1 \propto \hat{\mathbf{y}}$. We first consider parallel spin configurations. Figure 3(a) shows that the pair correlation is enhanced along the spin axis, indicating a pronounced axial attraction. When the spins are orthogonal [Fig. 3(b)], the correlations are again strongly anisotropic, but their maxima are localized in the upper-left and lower-right quadrants consistent with a spin-dependent transverse attraction. For antiparallel spins ($\theta_1 = \theta_2 + \pi$), the particles are likely to be in contact ($r = 2a$) in all directions yet the correlations exhibit a stronger left–right asymmetry [Fig. 3(c)]. The asymmetries in the correlations plotted in Figs. 3(b) and 3(c) directly reveal a nonreciprocal component of the effective interactions.

We now infer the symmetry of the effective spin interactions, through the angular pair-correlation function. Working in the reference frame where particle 1 is at the origin ($\mathbf{r}_1 = 0$), and $\boldsymbol{\omega}_1 \propto \hat{\mathbf{y}}$, we measure the probability that the two particles differ in spin orientation by an angle $\Delta\theta$ when they are separated by a vector $\mathbf{r}$: $C_{\boldsymbol{\omega}}(\Delta\theta|\mathbf{r}) = P(\theta_i - \theta_j = \Delta\theta|\mathbf{r}_2 - \mathbf{r}_1 = \mathbf{r})$. When the second particle lies in the direction transverse to $\boldsymbol{\omega}_1$, $C_{\boldsymbol{\omega}}$ peaks at $\Delta\theta = \pi$ [Fig. 3(d)], which indicates a preference for

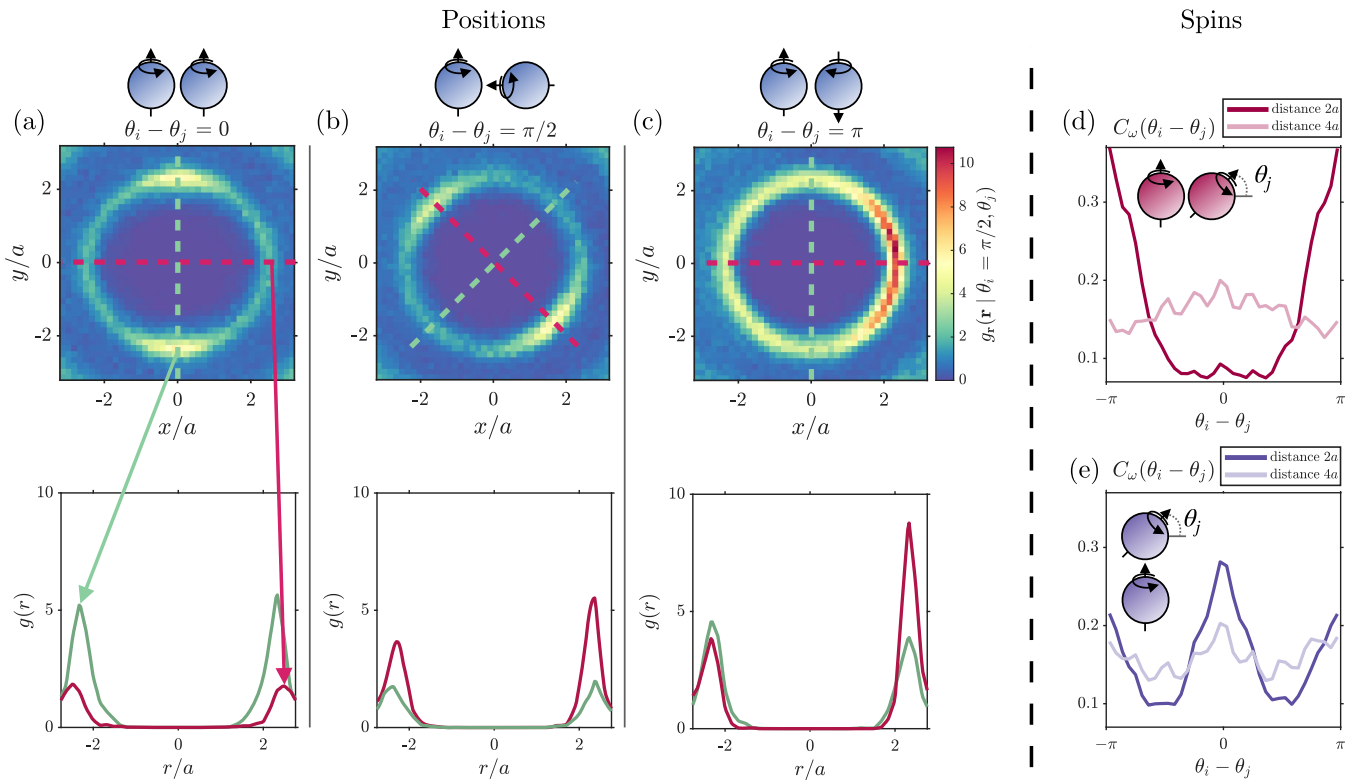


FIG. 3. From correlations to interactions. Top: Spin-resolved two-point distributions measured for different spin configurations ($g_{\mathbf{r}}(\mathbf{r}, \theta_1, \theta_2)$). Bottom: Directional cross sections of maps (a),(b), and (c) along the red and green dashed lines. (a) When the two spins $\boldsymbol{\omega_1}$ and $\boldsymbol{\omega_2}$ are aligned, the probability to find a second spinner is maximal in the axial direction. (b) When the two spins are orthogonal, the probability is maximal in the lower right and upper left quadrants. (c) When the two spins are anti-parallel, $g_{\mathbf{r}}$ features as strong peak at contact in all directions, but with pronounced the left-right asymmetry. (d) Position-resolved angular pair-correlation function for two spins sitting on the x axis ($C_{\boldsymbol{\omega}}$). The first spin $\boldsymbol{\omega_1}$ points along the y axis. The most probable configuration corresponds to anti-aligned spins at short distances. At distances larger than $5a$, we measure no spin correlations. (e) Same quantities measured when the spinners sit on the y axis. At short distance, the most probable configuration corresponds to spins pointing in the same direction. At long distance, the spin orientations are uncorrelated.

antiparallel alignment, and thus effective antiferromagnetic interactions in the transverse direction. Conversely, when the separation is axial, [Fig. 3(e)], $C_{\boldsymbol{\omega}}$ is maximal at $\Delta\theta = 0$, which echoes ferromagnetic alignment along the spin axis. In both cases, the correlations decay rapidly with increasing r, signaling that the effective spin interactions are short ranged.

The pair correlations $g_{\mathbf{r}}$ and $C_{\boldsymbol{\omega}}$ constrain the symmetry of the effective interactions, and reveal three essential features: a strong omnidirectional peak at contact, spin-dependent directional interactions, position-dependent spin alignment, and nonreciprocity. As detailed in Supplemental Material [21], such properties cannot result from the reciprocal forces between Quincke electrostatic dipoles [28,47]. They instead point toward dominant hydrodynamic couplings. However, the viscous flows induced by the spinning motion of Quincke spinners has already been shown to yield no attractive pumping in [28,48]. In the next section we show that this apparent contradiction is resolved by prominent inertial hydrodynamic interactions.

B. Inertial hydrodynamic interactions

To elucidate how hydrodynamics couples the internal and positional degrees of freedom, we recall that the Reynolds number associated with the vortex generated by a spinner exceeds 300, clearly placing the system in an inertial regime. Each spinner behaves as a localized vortical source, or "vortlet" [18], dressed with a secondary flow with a strong quadrupolar structure revealed by Fig. 4(a) and Supplemental Material [21], see also [4,18,20,49]. Centrifugal inertia and mass conservation generate transverse fluid expulsion and axial pumping around each spinner. This quadrupolar flow results in a strong axial advection towards the spinner, consistent with the pair correlations reported in Fig. 3(b). However, this inertial pumping is independent of the spin $\boldsymbol{\omega}_2$ of the second particle, and therefore cannot account for the full spin-dependent structure of the correlations $g_{\mathbf{r}}$ [Figs. 3(b) and 3(c)]. A crucial observation is that the particles are not merely advected by the flows. They are not a passive tracer, but actively spin while being advected by the flow generated by their

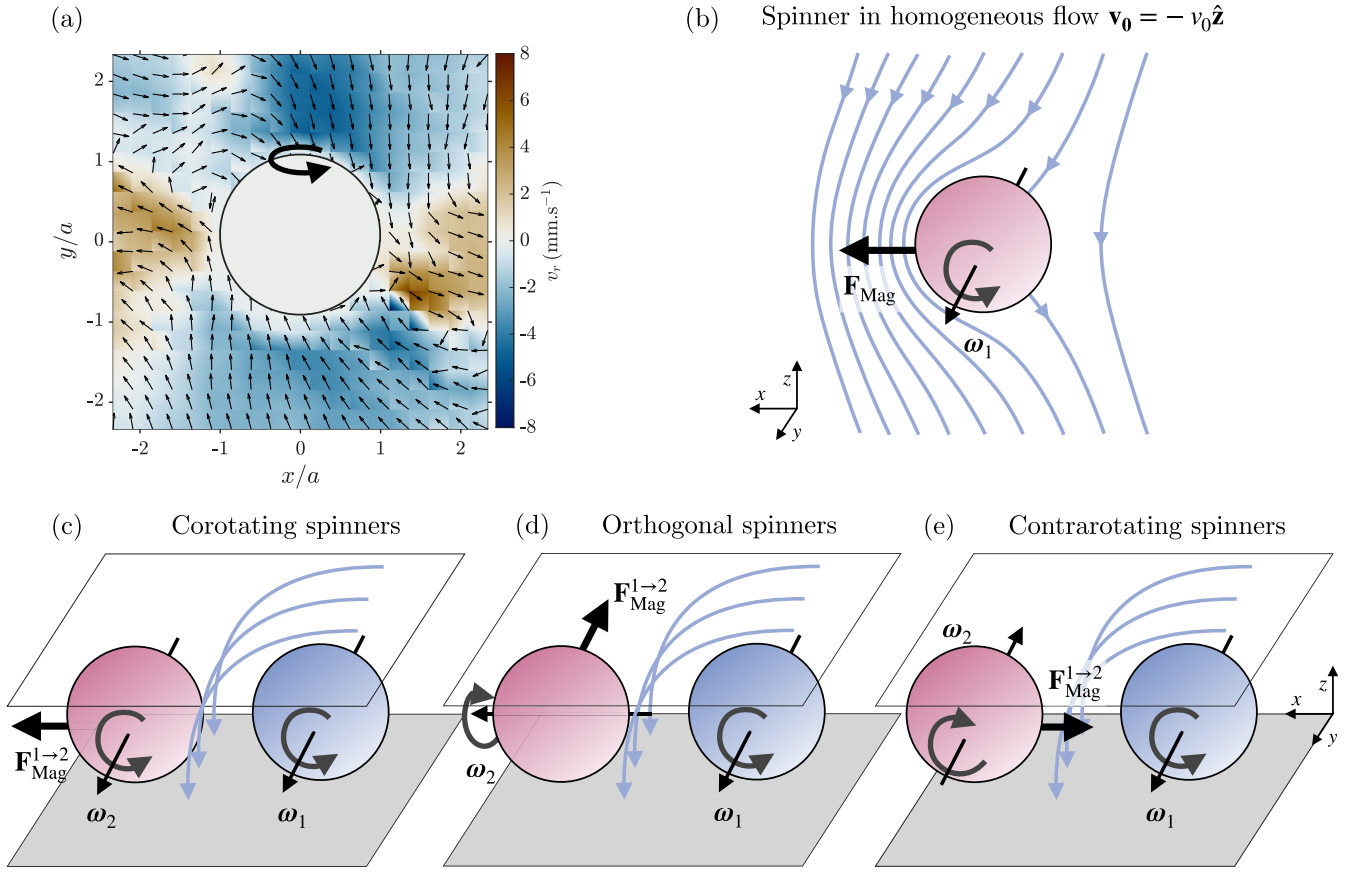


FIG. 4. Inertial pumping, Magnus forces, and (anti)aligning torques. (a) Velocity field measured by particle imaging velocimetry of the fluid flow averaged over the z direction around a spinner ($E = 8500$ V). Integrating over z, the main vortex contributions vanish revealing the secondary flow field. Centrifugal force expels the fluid in the transverse direction and mass conservation implies axial pumping. The left-right asymmetry is a consequence of the residual spinning motion. See Supplemental Material [21] for experimental details and for a detailed characterization. (b) Illustration of the Magnus effect acting on a spinner in a homogeneous flow. Because of the spinner's rotation, the flow is accelerated at the left the spinner and slowed down at the right, creating a net force to the left. (c) Resulting interaction between two corotating spinners. The resulting force of 2 on 1 is repulsive. (d) Resulting interaction between two orthogonal spinners. The resulting force of 2 on 1 is transverse. (e) Resulting interaction between two contrarotating spinners. The resulting force of 2 on 1 is attractive.

neighbors. Consequently, and as illustrated in Fig. 4(b), a particle with a spin $\boldsymbol{\omega}$ experiences a transverse lift, a Magnus force, $\mathbf{F}_{\mathrm{Mag}} = C\rho\mathbf{v}(\mathbf{r}) \times \boldsymbol{\omega}$ when the fluid of density ρ is locally moving at a velocity $\mathbf{v}(\mathbf{r})$ (C a geometrical factor of order a^3) [50,51]. This phenomenon leads to counterintuitive hydrodynamic interactions. For separations smaller than the electrode spacing, and ignoring secondary-flow corrections, we can approximate the vortex generated by a spinner rotating with $\boldsymbol{\omega}_1$ as $\mathbf{v}_1(\mathbf{r}) = (a/r)^3\boldsymbol{\omega}_1 \times \mathbf{r}$ (at larger distances the vortex is exponentially attenuated by confinement) [19]. Substituting this expression into the Magnus force yields the interaction force

$$\mathbf{F}^{1\to2}_{\mathrm{Mag}} = C\left(\frac{a}{r_{12}}\right)^3 \rho(\boldsymbol{\omega}_1 \times \mathbf{r}_{12}) \times \boldsymbol{\omega}_2, \qquad (1)$$

which exceeds the viscous drag by orders of magnitude (see Supplemental Material [21]). This formula immediately reveals three key properties. First, Magnus interactions depend on both particle spins, demonstrating explicitly that the positional dynamics is directly coupled to the internal spin degrees of freedom. Second, these interactions feature an action-reaction symmetry only when the two spins are collinear as $\mathbf{F}^{1\to2}_{\mathrm{Mag}} + \mathbf{F}^{2\to1}_{\mathrm{Mag}} \propto (\boldsymbol{\omega}_1 \times \boldsymbol{\omega}_2) \times \mathbf{r}_{12}$. Finally, when the spins are orthogonal, the Magnus forces either vanish or become purely transverse to the separation vector $\mathbf{r_{12}}$.

These remarkable properties provide a natural interpretation of the measured pair correlations from the joint action of inertial pumping and Magnus force (Fig. 3): (i) When the spins are parallel, Eq. (1) predicts that the Magnus force is purely repulsive along the direction normal to the spins [Fig. 4(c)]. Combined with the axial pumping induced by the inertial vortical flow, this mechanism

accounts for the strong anisotropic structure observed in Fig. 3(a). (ii) When the spins are orthogonal, Eq. (1) predicts forces that are either vanishing or purely transverse [Fig. 4(d)]. A second particle can approach a spinner only when it lies in its upper-left or lower-right quadrants. Combined with contact repulsion this interaction is again consistent with the tilted correlations reported in Fig. 3(b). (iii) The strong contact peak observed for antiparallel spins [Fig. 3(c)] provides the final and most restrictive test of the interaction mechanisms. It cannot result from inertial pumping alone, as it expels fluid transversely, or from electrostatic dipolar interactions, which are repulsive for any dipole tilt. Purely viscous interactions cannot explain the contact peak either as they do not yield any centripetal pumping [28,48]. Residual rolling can account for the left-right asymmetry, but not for the dominant inversion-symmetric component of the pair correlations. They therefore rely on an additional (transverse) attractive mechanism: Magnus forces [Fig. 4(e)]. Equation (1) predicts precisely such an attraction for antiparallel spins, while predicting transverse repulsion for parallel spins, consistently with the contrast between Figs. 3(a) and 3(c), and the spinner pairing reported in [18,19].

Having established how particle spins shape the effective interparticle forces, we now turn to the reciprocal problem: how the torques acting on the spins depend on particle positions. Elucidating this mechanism closes the feedback loop that couples the rotational and positional degrees of freedom of the spinners. To understand how spins interact, it is useful to recall that Quincke rotation originates from an instability that spontaneously breaks the rotational symmetry of the electro-hydrodynamic problem. As a result, an isolated Quincke particle can rotate around any axis lying in the plane perpendicular to the applied electric field [47]. An external torque explicitly breaks this symmetry and selects the stationary rotation axis [30], in direct analogy with the alignment of an XY spin in a magnetic field. Consider a spinner located at the origin and rotating with angular velocity $\boldsymbol{\omega}_1 = \omega\hat{\mathbf{y}}$. At short distance, the lubrication flow it generates induces a hydrodynamic torque on a second spinner located at $\mathbf{r}$: $\mathbf{T}_2 = (X^C\mathbf{P} + Y^C\mathbf{P}^\perp)\cdot\boldsymbol{\omega}_1$, where $X^C > 0$ and $Y^C < 0$ are two constants and $\mathbf{P}$ and $\mathbf{P}^\perp$ are the projection operators on the $\mathbf{r}$ and $\mathbf{r}^\perp$ directions, see Supplemental Material [21] for details and [52]. This torque sets the direction of $\boldsymbol{\omega}_2$, and its direction depends on the relative position of the two particles. When the spinners are aligned along the rotation axis, the shear flow between them favors corotation, resulting in a ferromagnetic coupling. By contrast, when the particles are separated along the x axis, rolling interactions orient $\boldsymbol{\omega}_2$ opposite to $\boldsymbol{\omega}_1$ (see Supplemental Material [21]). These hydrodynamic interactions therefore produce position-dependent spin couplings that directly account for the symmetry of the spin-spin correlation functions $C_{\boldsymbol{\omega}}$ reported in Figs. 3(d) and 3(e). The hydrodynamic feedback loop is closed.

IV. FROM PAIR INTERACTIONS TO PHASE BEHAVIOR

Having established the structure and symmetries of pair interactions, we can now rationalize the phase behavior reported in Figs. 1 and 2. At low packing fractions the spatial organization of the suspension results from the competition between two nonequilibrium mechanisms. Inertial pumping produces a strongly anisotropic attraction along the spin axis. They effectively endow the particles with patchy interactions that promote the formation of directed bonds [Fig. 4(a)], see also [53]. In contrast, the nonreciprocal Magnus forces, and residual rolling motion, tend to disrupt these axial bonds, or to reorient them when the spin directions differ [Figs. 3(b), 3(c) and 4(b)]. This competition is reminiscent of the physics of equilibrium patchy colloids, where directional attractions compete with thermal fluctuations [32,36,54]. In those systems the finite valence of the interactions suppresses bulk phase separation and instead stabilizes percolating fluid or empty liquid phases. Although our spinners are neither Brownian nor in equilibrium, transverse motions induced by Magnus forces play a role analogous to thermal noise by continuously breaking and rearranging the bond network. As a result, inertial attraction promotes the formation of clusters. At the same time, the strong anisotropy of the interactions limits the effective valence of the spinner attraction, and prevents bulk phase separation and condensation into compact drops before connectivity percolates at system-spanning scales.

Unlike at low packing fraction, the collapse of the active percolating fluid into a spin-textured crystal above ϕ_x relies both on spin-dependent forces and on position-dependent spin interactions. At high density the feedback between particle positions and spin orientations becomes strong enough to arrest the spin dynamics. Instead of continuously reorienting, the spins freeze into ferro-antiferro configurations along the axial and transverse directions. In these configurations the Magnus forces that previously disrupted directed bonds vanish by symmetry. As a result, they no longer generate transverse rearrangements and instead contribute purely axial and lateral attractions between neighboring spinners [Fig. 3(c)]. The effective valence of the interactions therefore increases dramatically, and no dynamical mechanism remains capable of breaking the bonds between particles. Under these conditions phase separation becomes unavoidable: the percolating active fluid collapses into a dense phase of monodisperse spinners whose cohesion is reinforced by the emergent spin order, which simultaneously freezes the positional and orientational degrees of freedom. The resulting crystal can coexist with a dilute and isotropic liquid phase composed of finite clusters.

V. CONCLUSION AND OUTLOOK

Our experiments reveal a regime of active matter in which inertial hydrodynamics, rather than dissipation alone

governs collective organization. They highlight how feedback between flows and active degrees of freedom can control phase transitions and structural order, here through an effective patchiness leading to percolating fluids and spin-textured crystals. Looking ahead, exploring stronger driving conditions may uncover even richer dynamics, where active particles and inertial turbulence interact and organize one another.

ACKNOWLEDGMENTS

We thank W. Irvine, J. Lintuvuori, A. Snezhko, and N. Oppenheimer for insightful feedback and discussions. This project received funding from the European Research Council (ERC) under the European Union's Horizon 2020 research and innovation program (Grant Agreement No. 101019141) (D. B.).

DATA AVAILABILITY

There are no publicly available research data or software supporting this manuscript. Requests for further information or data should be sent to the authors.

[1] J. M. Crowley, *Clumping instability of a falling horizontal lattice*, Phys. Fluids **19**, 1296 (1976).
[2] B. A. Grzybowski, H. A. Stone, and G. M. Whitesides, *Dynamic self-assembly of magnetized, millimetre-sized objects rotating at a liquid–air interface*, Nature (London) **405**, 1033 (2000).
[3] É. Guazzelli and J. Hinch, *Fluctuations and Instability in Sedimentation*, Annu. Rev. Fluid Mech. **43**, 97 (2011).
[4] Y. Goto and H. Tanaka, *Purely hydrodynamic ordering of rotating disks at a finite Reynolds number*, Nat. Commun. **6**, 5994 (2015).
[5] M. Driscoll, B. Delmotte, M. Youssef, S. Sacanna, A. Donev, and P. Chaikin, *Unstable fronts and motile structures formed by microrollers*, Nat. Phys. **13**, 375 (2017).
[6] N. Oppenheimer, D. B. Stein, and M. J. Shelley, *Rotating Membrane Inclusions Crystallize Through Hydrodynamic and Steric Interactions*, Phys. Rev. Lett. **123**, 148101 (2019).
[7] R. Chajwa, N. Menon, S. Ramaswamy, and R. Govindarajan, *Waves, Algebraic Growth, and Clumping in Sedimenting Disk Arrays*, Phys. Rev. X **10**, 041016 (2020).
[8] H. Massana-Cid, D. Levis, R. J. H. Hernández, I. Pagonabarraga, and P. Tierno, *Arrested phase separation in chiral fluids of colloidal spinners*, Phys. Rev. Res. **3**, L042021 (2021).
[9] E. S. Bililign, F. Balboa Usabiaga, Y. A. Ganan, A. Poncet, V. Soni, S. Magkiriadou, M. J. Shelley, D. Bartolo, and W. T. Irvine, *Motile dislocations knead odd crystals into whorls*, Nat. Phys. **18**, 212 (2022).
[10] T. H. Tan, A. Mietke, J. Li, Y. Chen, H. Higinbotham, P. J. Foster, S. Gokhale, J. Dunkel, and N. Fakhri, *Odd dynamics of living chiral crystals*, Nature (London) **607**, 287 (2022).
[11] Z. Shen and J. S. Lintuvuori, *Collective flows drive cavitation in spinner monolayers*, Phys. Rev. Lett. **130**, 188202 (2023).
[12] S. Guillet, A. Poncet, M. Le Blay, W. T. Irvine, V. Vitelli, and D. Bartolo, *Melting of nonreciprocal solids: How dislocations propel and fission in flowing crystals*, Proc. Natl. Acad. Sci. U.S.A. **122**, e2412993122 (2025).
[13] T. Pedley and J. O. Kessler, *Hydrodynamic phenomena in suspensions of swimming microorganisms*, Annu. Rev. Fluid Mech. **24**, 313 (1992).
[14] D. Saintillan and M. J. Shelley, *Instabilities and pattern formation in active particle suspensions: Kinetic theory and continuum simulations*, Phys. Rev. Lett. **100**, 178103 (2008).
[15] T. Sanchez, D. T. Chen, S. J. DeCamp, M. Heymann, and Z. Dogic, *Spontaneous motion in hierarchically assembled active matter*, Nature (London) **491**, 431 (2012).
[16] M. C. Marchetti, J.-F. Joanny, S. Ramaswamy, T. B. Liverpool, J. Prost, M. Rao, and R. A. Simha, *Hydrodynamics of soft active matter*, Rev. Mod. Phys. **85**, 1143 (2013).
[17] A. Doostmohammadi, J. Ignés-Mullol, J. M. Yeomans, and F. Sagués, *Active nematics*, Nat. Commun. **9**, 3246 (2018).
[18] P. Chen, S. Weady, S. Atis, T. Matsuzawa, M. J. Shelley, and W. T. Irvine, *Self-propulsion, flocking and chiral active phases from particles spinning at intermediate Reynolds numbers*, Nat. Phys. **21**, 146 (2025).
[19] M. Gelvan, A. Chirko, J. Kirpitch, Y. Lavie, N. Israel, and N. Oppenheimer, *Hydrodynamic spin-pairing and active polymerization of oppositely spinning rotors*, Nat. Commun. **16**, 10368 (2025).
[20] Z. Shen, D. Fu, and J. S. Lintuvuori, *Inertia-driven propulsion of asymmetric spinner-dimers at moderate Reynolds numbers 21*, Soft Matter **21**, 4021 (2025).
[21] See Supplemental Material at http://link.aps.org/supplemental/10.1103/xyym-pjh7 for experimental and analysis methods, the rolling-to-hovering crossover, the exclusion of motility-induced phase separation, relaxation dynamics in the holey-liquid phase, hydrodynamic and electrostatic torques, estimates of the Magnus force, and supplemental videos, which includes Refs. [22–26].
[22] A. Chardac, L. A. Hoffmann, Y. Poupart, L. Giomi, and D. Bartolo, *Topology-driven ordering of flocking matter*, Phys. Rev. X **11**, 031069 (2021).
[23] D. Blair and E. Dufresne, *The MATLAB particle tracking code repository*, Particle-tracking code available at http://physics.georgetown.edu/matlab (2008).
[24] J. C. Crocker and D. G. Grier, *Methods of digital video microscopy for colloidal studies*, J. Colloid Interface Sci. **179**, 298 (1996).
[25] W. Thielicke and R. Sonntag, *Particle image velocimetry for MATLAB: Accuracy and enhanced algorithms in PIVlab*, J. Open Res. Software **9**, 12 (2021).
[26] L. D. C. Jaubert, M. Haque, and R. Moessner, *Analysis of a fully packed loop model arising in a magnetic coulomb phase*, Phys. Rev. Lett. **107**, 177202 (2011).
[27] G. Quincke, *Ueber rotationen im constanten electrischen felde*, Ann. Phys. (Berlin) **295**, 417 (1896).
[28] A. Bricard, J.-B. Caussin, N. Desreumaux, O. Dauchot, and D. Bartolo, *Emergence of macroscopic directed motion in*

populations of motile colloids, Nature (London) **503**, 95 (2013).
[29] G. E. Pradillo, H. Karani, and P. M. Vlahovska, *Quincke rotor dynamics in confinement: Rolling and hovering*, Soft Matter **15**, 6564 (2019).
[30] R. Braun, A. Poncet, A. Morin, and D. Bartolo, *Phase coherence and disorder-induced wave propagation in micromotor arrays*, Nat. Phys. (2026).
[31] C. P. Royall, M. A. Faers, S. L. Fussell, and J. E. Hallett, *Real space analysis of colloidal gels: Triumphs, challenges and future directions*, J. Phys. Condens. Matter **33**, 453002 (2021).
[32] F. Sciortino and E. Zaccarelli, *Reversible gels of patchy particles*, Curr. Opin. Solid State Mater. Sci. **15**, 246 (2011).
[33] I. Buttinoni, J. Bialké, F. Kümmel, H. Löwen, C. Bechinger, and T. Speck, *Dynamical clustering and phase separation in suspensions of self-propelled colloidal particles*, Phys. Rev. Lett. **110**, 238301 (2013).
[34] M. E. Cates and J. Tailleur, *Motility-induced phase separation*, Annu. Rev. Condens. Matter Phys. **6**, 219 (2015).
[35] F. Ginot, I. Theurkauff, F. Detcheverry, C. Ybert, and C. Cottin-Bizonne, *Aggregation-fragmentation and individual dynamics of active clusters*, Nat. Commun. **9**, 696 (2018).
[36] E. Zaccarelli, *Colloidal gels: Equilibrium and non-equilibrium routes*, J. Phys. Condens. Matter **19**, 323101 (2007).
[37] E. Tjhung, C. Nardini, and M. E. Cates, *Cluster phases and bubbly phase separation in active fluids: Reversal of the Ostwald process*, Phys. Rev. X **8**, 031080 (2018).
[38] M. Sanoria, R. Chelakkot, and A. Nandi, *Percolation transition in phase-separating active fluid*, Phys. Rev. E **106**, 034605 (2022).
[39] G. Fausti, M. E. Cates, and C. Nardini, *Statistical properties of microphase and bubbly phase-separated active fluids*, Phys. Rev. E **110**, L042103 (2024).
[40] L. Yao and R. L. Jack, *Interfacial and density fluctuations in a lattice model of motility-induced phase separation*, J. Chem. Phys. **162**, 114902 (2025).
[41] E. Bianchi, J. Largo, P. Tartaglia, E. Zaccarelli, and F. Sciortino, *Phase diagram of patchy colloids: Towards empty liquids*, Phys. Rev. Lett. **97**, 168301 (2006).
[42] B. Nienhuis, *Critical behavior of two-dimensional spin models and charge asymmetry in the Coulomb gas*, J. Stat. Phys. **34**, 731 (1984).
[43] D. Stauffer, *Scaling theory of percolation clusters*, Phys. Rep. **54**, 1 (1979).
[44] H. Saleur and B. Duplantier, *Exact determination of the percolation hull exponent in two dimensions*, Phys. Rev. Lett. **58**, 2325 (1987).
[45] B. Duplantier and H. Saleur, *Exact critical properties of two-dimensional dense self-avoiding walks*, Nucl. Phys. **B290**, 291 (1987).
[46] A. J. Bray, *Theory of phase-ordering kinetics*, Adv. Phys. **51**, 481 (2002).
[47] J. Melcher and G. Taylor, *Electrohydrodynamics: A review of the role of interfacial shear stresses*, Annu. Rev. Fluid Mech. **1**, 111 (1969).
[48] B. Zhang, H. Yuan, A. Sokolov, M. O. De La Cruz, and A. Snezhko, *Polar state reversal in active fluids*, Nat. Phys. **18**, 154 (2022).
[49] W. Bickley, *The secondary flow due to a sphere rotating in a viscous fluid*, London Edinburgh Dublin Philos. Mag. J. Sci. **25**, 746 (1938).
[50] S. I. Rubinow and J. B. Keller, *The transverse force on a spinning sphere moving in a viscous fluid*, J. Fluid Mech. **11**, 447 (1961).
[51] E. Guyon, J. P. Hulin, L. Petit, and C. D. Mitescu, *Physical Hydrodynamics* (Oxford University Press, New York, 2015).
[52] D. Jeffrey and Y. Onishi, *Calculation of the resistance and mobility functions for two unequal rigid spheres in low-Reynolds-number flow*, J. Fluid Mech. **139**, 261 (1984).
[53] P. Gondret and L. Petit, *Viscosity of periodic suspensions*, Phys. Fluids **8**, 2284 (1996).
[54] J. Russo, F. Leoni, F. Martelli, and F. Sciortino, *The physics of empty liquids: From patchy particles to water*, Rep. Prog. Phys. **85**, 016601 (2022).